Digest Journal of Nanomaterials and Biostructures Vol. 18, No. 1, January - March 2023, p. 131 - 143

Characterization of pure and Cu doped V_2O_5 nanostructures and their $Cu:V_2O_5$/p-Si photodiode applications

N. S. Kumar[a], B. Babu[b,*], M. Gowtham[a], C. Sivakumar[b,c], M.S. Ho[b,c], J. H. Chang[d], K. Mohanraj[d,*]

[a]*Department of Physics, Kongunadu Arts and Science College, Coimbatore-641029 Tamil Nadu, India*

[b]*Department of Physics, National Chung Hsing University, Taichung 40227, Taiwan*

[c]*Innovation and Development Center of Sustainable Agriculture (IDCSA), National Chung Hsing University, Taichung, 40227, Taiwan*

[d]*Department of Environmental Engineering and Management, Chaoyang University of Technology, Taichung 413310, Taiwan*

In this study, a wet chemical approach was exploited to synthesis of Cu-doped V_2O_5 (CVO) nanostructures with different doping concentrations of Cu at 5, 10, and 15%. The structural analysis confirms that samples annealed at 600°C rehabilitated to monoclinic V_2O_5. The surface morphology and nanostructure were studied by SEM and TEM analysis. The presence of various elements (Cu, V & O) and their compositions were confirmed using EDS and XPS measurements. The photoluminescence spectrum reveals a strong blue emission at 418 nm is ascribed to the electronic transition from vanadium interstitial to the valence band. Further, we fabricated the junction diodes by the nebulizer spray depositing CVO nanostructures in a colloidal form on the p-Si substrate at 150°C. Depending on the applied voltage and Cu doping level the rectifying behavior with a high rectification ratio (RR) was observed from the I-V characteristics of studied diodes. Inclusively, a V_2O_5 with substitution of Cu at.15% has significantly enhanced the photoresponse time and current density ($J=4.19x10^{-4}A/cm^2$).

(Received July 23, 2022; Accepted January 24, 2023)

Keywords: V_2O_5, Phase change, Doping, Morphological, Schottky diode

1. Introduction

Vanadium is a common element in the earth's crust, so it can exist in a wide range of valence states. It exists as vanadium monoxide (VO), vanadium sesquioxide (V_2O_3), vanadium dioxide, and vanadium pentoxide (V_2O_5) as a single valence oxide form in the oxidation states V^{2+} to V^{5+}. Conditions such as temperature and pressure affect the oxidation states of vanadium as well as the phase and concentration of vanadium [1]. Recent interest in V_2O_5 as a microelectronic and optoelectronic device semiconductor has grown significantly [2]. For photodetection applications, it has a promising band gap in the visible light region (Eg=2.2-2.7eV) [2], which makes it an optoelectronic device-useable material. Furthermore, oxides have the potential to serve as host materials for the implantation of rare earth ions due to their oxygen inclusion and wide bandgap nature, which improves photoluminescence emission [3-5]. Transition metal oxides have received a lot of attention due to their high work function, semiconducting nature, and excellent transparency. Transition metal oxides such as vanadium pentoxide, molybdenum trioxide, titanium dioxide, cerium oxide and tungsten trioxide are used in organic light-emitting diodes, buffer layers for photovoltaic devices, and other solid-state electronic devices [6-13]. Optical V_2O_5 has the following properties: direct optical energy gap, good chemical properties, thermal stability, and excellent specific energy in an orthorhombic layered structure. Infrared sensors [14], gas sensors [15], catalysts [16], and optoelectronic devices [17] are just a few of the applications where V_2O_5 has emerged as a promising material. Photodetectors (PDs) such as Schottky diodes [18], p–n

---

* Corresponding author: mohan1991mpt@gmail.com
https://doi.org/10.15251/DJNB.2023.181.131

junctions [19], photoconductors [20] and MSM type [21] are used for light detection. In this route, exploits are proposed to extend morphology and composition, and it is well controlled. Doping is one of the influential approaches to accumulating optical and electrical properties. Its functioning purpose is to influence the substitution ions of defects into parent material, which influences the lower or upper level band tuned by Eg. Several metal ions, namely Al, Co, Ag, and Ni, have been widely reported for V_2O_5 doping [22-24]. By altering V_2O_5's electronic structure or increasing its activity, metal substitution can produce drastic changes in the material's optical, electrical, and magnetic properties. One of the most difficult problems to solve is how to make metal oxides more electrically and optically conductive. Other than these methods of improving optical, electrical, and magnetic properties, metal oxides can be alloyed with appropriate elements. The wide bandgap engineering (i.e. inducing defects) in a V_2O_5 lattice can be increased by using an extrinsic dopant (Al, Zn, Cu, W, Co, and so on) as a donor, which improves the electrical and optical properties of V_2O_5. [25–29] It has good surface morphology even at high doping levels, a moderate number of deep level traps, and low memory effects to improve material properties. Cu is a significant common dopant. The different metal ions, Cu, get much interest owing to their similar electronic shell structure, physical and chemical properties to those of V_2O_5. The present work is detailed in the study of pure and Cu-doped V_2O_5. The outcome of the Cu^{2+} ion concentration on the physical, morphological, optical, and electrical features of V_2O_5 is being studied. With the intention of realizing these, an effort has been made to pronounce a solution-processed fabricated diode in the architecture of Ag/Cu doped V_2O_5 /p-Si/Ag. Electrical features of the device's performance were studied to determine the impact of varied Cu^{2+} substitutions and establish an efficient UV photodiode ability

2. Materials and experimental procedure

2.1. Preparation of Cu-V_2O_5 nanostructures

The analytical grade (AR) of ammonium metavanadate and copper nitrate were used as starting materials. The stoichiometric amount of the above-mentioned starting ingredients [NH_4VO_3 and $Cu(NO_3)_2$] were dissolved separately in 40 ml of deionized water (DI) under stirring in a conventional synthesis method. Cu concentrations of 5, 10, and 15% were set, and the precursor solutions were quickly mixed to make a homogeneous mixture. Then, over the course of 20 minutes at room temperature, 1M of H_2O_2 solution was added dropwise to the aforesaid combination. Instantly, ions were formed as a milky white to dull orange precipitate. Then, 0.2 mol/L HNO_3 was slowly dropped into the above solution until the pH value reached at 2 under continuous stirring. After continuously stirred for 30 min, the suspension was added with a slight quantity of PVP. The surfactant solution was added to the container of the final solution, and it's kept in a hot plate at the temperature of 50°C for 12 h. Afterwards, the obtained dull blueish precipitates were collected by centrifugation and washed with DI water, ethanol and acetone to extract the remaining ions from the final product and calcined at 600°C for 1 h. The undoped V_2O_5 sample was prepared in the same manner as described above without Cu doping.

2.2. Characterization techniques

The structural properties of pure and CVO samples were investigated via an X-ray diffraction system (D8 AXS, Bruker) with CuKα radiation (λ=1.5406Å). Surface morphology was detected through SEM (JEOL-Model JSM-6390LV)/High-resolution transmission electron Microscopy (HRTEM, TECHNAI T20). The elemental composition studies were performed over and done with energy dispersive X-ray spectroscopy with X-ray studies incorporated into an SEM instrument. Photoluminescence of the investigated samples was recorded using Horiba Jobin Yuon Fluorolog with a wavelength range of 185-900 nm. The diode's I-V characteristics under dark and illumination were performed using a Keithley (model 6517 B) source meter. During photocurrent measurements, a UV light source with a wavelength of 365 nm and a power density of 0.3 mW/cm^2 was used as an excitation source.

3. Results and discussion

3.1. Structural analysis

Figure 1(a-b) depicts the XRD pattern of pure and Cu-doped V_2O_5 (Cu at. 5, 10 and 15%) samples annealed at 600°C for 1 h. The intense peaks at 2θ=15.47, 20.39, 26.27 and 31.14o corresponds to (200), (001), (110) and (400) crystal planes, respectively. All the observed peaks are well matched to JCPDS card No.: 41-1426 with lattice parameters, a = 11.51 Å, b = 3.565 Å and c = 4.372 Å. In this pattern shows an additional peak at 2θ values of 26.89^o, 28.13^o and 30.35^o (marked by star *) are associated with a monoclinic phase of ε-$Cu_{0.85}V_2O_5$.

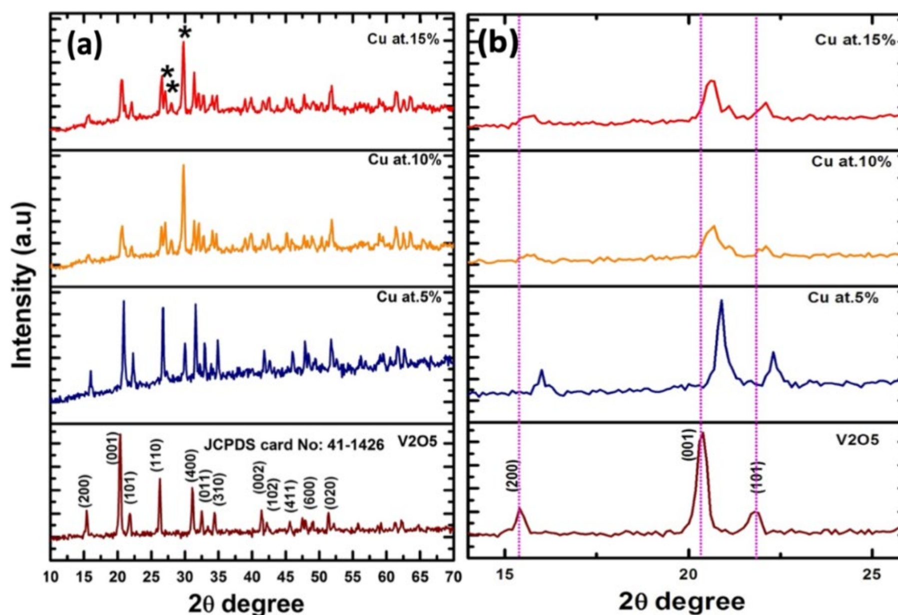

Fig. 1. XRD spectrum of (a) $Cu_xV_2O_5$ annealed at 600°C and (b) peak shift position of the $Cu_xV_2O_5$.

Table 1. Structural parameters of the pure and $Cu_xV_2O_5$ samples annealed at 600 °C for 1 h.

	2θ (degree)	hkl	d-spacing (nm)	FWHM (degree)	Crystallite size (D) (nm)	Lattice parameters (Å)			Dislocation density (10^{14} lines/m^2)	Micro-strain (ε) 10^4lin^{-2}m^{-4}
						a	b	c		
	$Cu_xV_2O_5$ (x=0)									
	15.4136	200	5.74406	0.31750	25.2620				0.001567	0.159152
00	20.3600	001	4.35865	0.33750	23.9268				0.001747	0.167283
	26.2487	110	3.39242	0.29870	27.3226	11.48	3.555	4.358	0.001340	0.177739
	51.3571	020	1.77766	0.27460	32.1134				0.000970	0.190126
	$Cu_xV_2O_5$ (x=5)									
	15.2934	200	5.78893	0.52970	15.1398				0.004363	0.131241
05	20.0700	001	4.42067	0.38000	21.2412				0.002216	0.162620
	26.7241	110	3.33314	0.28260	28.9074	11.57	3.526	4.420	0.001197	0.179334
	51.8092	020	1.76321	0.34960	25.2722				0.001566	0.187530
	$Cu_xV_2O_5$ (x=10)									
	15.6594	200	5.65444	0.52950	15.1521				0.004356	0.132895
10	20.5957	001	4.30900	0.40760	19.8192				0.002546	0.160946
	26.4951	110	3.36142	0.31740	25.7258	11.30	3.526	4.309	0.001511	0.176569
	51.8132	020	1.76308	0.42150	20.9616				0.002276	0.184948
	$Cu_xV_2O_5$ (x=15)									
	15.6271	200	5.66606	0.54120	14.8239				0.004551	0.131266
15	20.6173	001	4.30454	0.47130	17.1410				0.003403	0.154875
	26.4935	110	3.36162	0.34840	23.4367	11.33	3.530	4.304	0.001821	0.174269
	51.7380	020	1.76547	0.51050	17.3016				0.003341	0.181718

On increasing the dopant concentration at Cu at. 5 to 10%, the respective additional peaks intensity is also increased. When compared to undoped V_2O_5, the primary diffraction peaks of Cu^{2+} samples move toward a higher angle (2θ), as seen in Fig. 1(b). This shift in the patterns depicts that Cu^{2+} ions were substituted for V^{5+} sites since the ionic radius of Cu^{2+} (0.57 Å) was higher than that of V^{5+} (0.54 Å) [30]. The crystallite size of studied samples is determined from intense peaks of diffraction using Debye-Scherrer's equation [31]. The estimated crystallite size of pure V_2O_5 is 25.26 nm, which decreases with increasing Cu^{2+} concentration (listed in Table 1). External contaminants (i.e., Cu^{2+}) distort the host V^{5+} lattice, resulting in a reduction in the nucleation and subsequent growth rate of the V_2O_5 nanoparticles.

3.2 SEM-EDS analysis

A larger amount of regular and unique rod mixed with a few disk nanostructures appeared when the prepared samples calcinated at 600°C for 12 hrs are shown in 2(a-d). This indicates that the surface diffusion phenomenon is significant in the thermal growth of nanorods. Fig 2(a) depicts the formation of nanorods of undoped V2O5 with long blunt ends resembling a hexagonal face. Still the nanorods dimension became smaller while the increase of the Cu doping concentration (Fig. 2(b-d)). This could be attributed to rapid growth along the (001) axis, as Cu-doping can promote V_2O_5 growth along the C axis. At 5% Cu-doping, more uniform straight nanorods with the smallest diameter are found over a large area. The large distortion influenced the natural growth behaviour of the nanorods array, resulting in the formation of disk-like particles in addition to nanorods at 10% Cu-doping. When Cu is introduced at 15% and its dipolar interaction along the

c-axis, the progress of nanorods is exchanged by dense interconnected disk-like structures. EDS analysis revealed the presence of vanadium and oxygen in V_2O_5 samples, while Cu-doped V_2O_5 samples revealed the presence of copper as well as vanadium and oxygen. The presence of V, O, and Cu elements and high purity of pure and CVO samples annealed at 600^oC for one hour are addressed by the EDS analysis in Fig. 2(e-h).

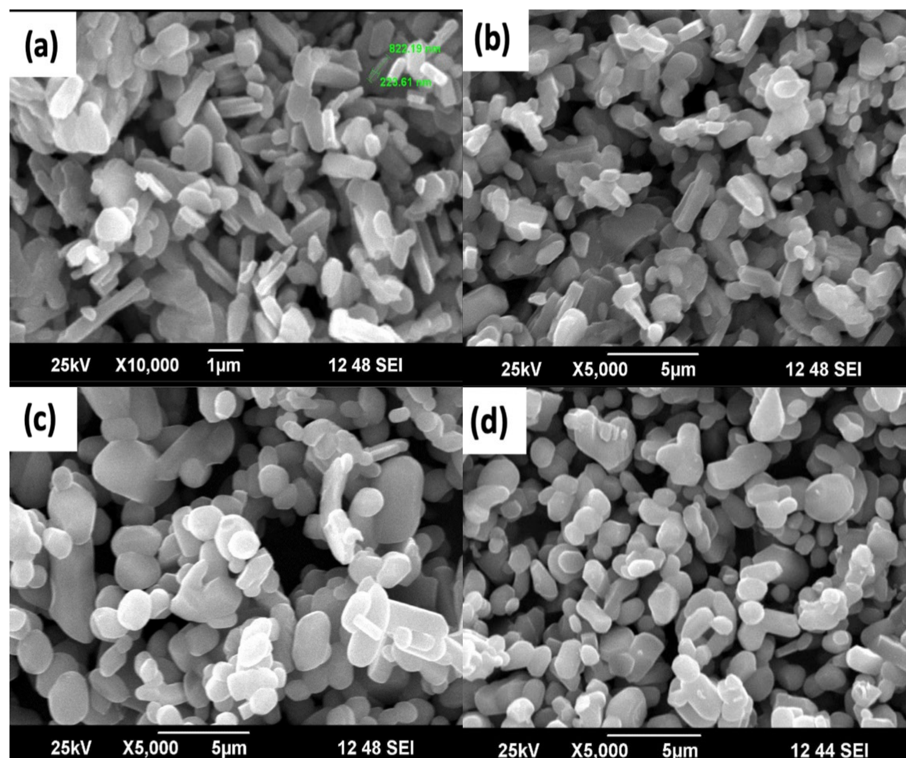

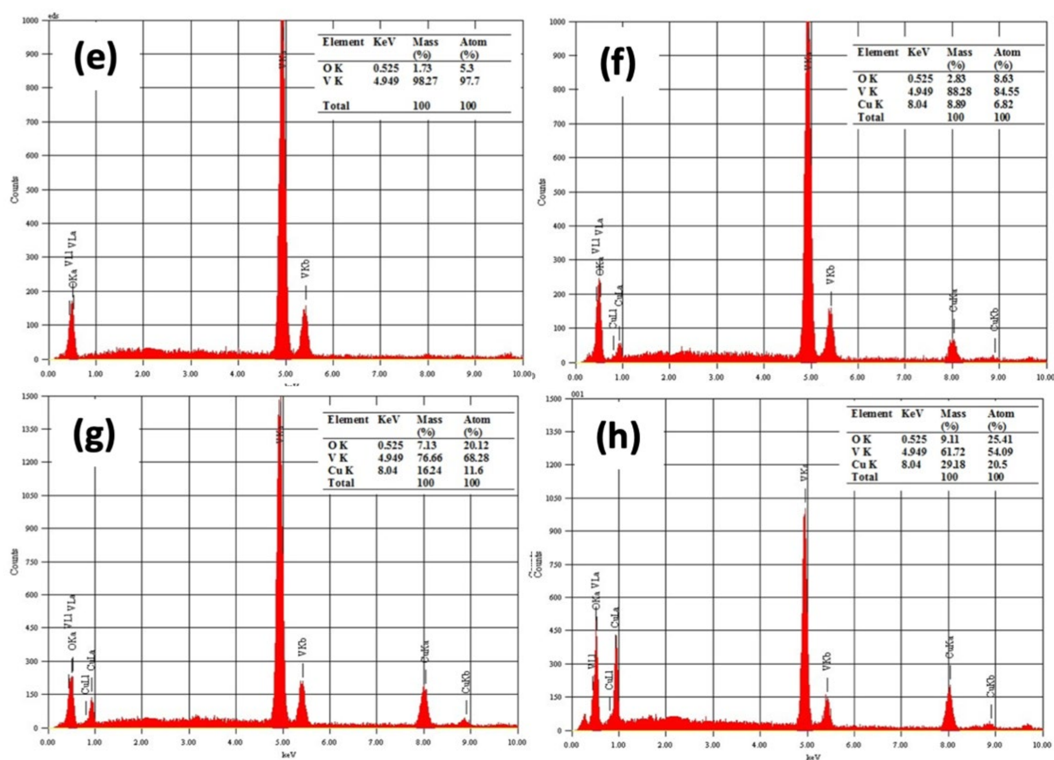

Fig. 2 SEM images of (a-d) pure and $Cu_xV_2O_5$ samples and EDS spectra of (e-h) pure and $Cu_xV_2O_5$.

3.3 TEM analysis

Fig. 3(a-d) shows the TEM images of pure and CVO nanorods together with their SAED patterns. In figure 3(a), the pure V_2O_5 nanorods show a morphology with an average diameter of 290 and length of 862 nm. The HRTEM image of a distinct nanorod exhibit that lattice fringes are continuous over a long distance with no crystal disorder. The lattice fringes are clearly separated by 0.479 nm of d-spacing, which is related to the (200) plane of orthorhombic V_2O_5 [32]. The diffraction bright areas in the SAED pattern can be indexed to the (200) plane for the orthorhombic phase of V_2O_5 in the inset left-bottom of Fig. 3 (a). Figure 3(b-d) shows TEM images of CVO samples, and the average length and diameter of the (Cu at.5%) nanorods are 0.7 and 1.38 m, respectively. Furthermore, as the doping concentration at Cu increases from 10% to 15%, aggregates of rods with disk-like particles are discovered, with average lengths of 0.74±4 m and 493±4 nm, respectively. Nonetheless, a careful examination of the TEM analysis reveals that the particle size decreases progressively as the concentration of the dopant ions increases. It is clear from Fig. 3 (b-d) that the samples are made up of nanorods mixed with disk-like particles with a uniform size distribution and a high degree of agglomeration. The inset SAED patterns comprised of bright spot patterns in this figure implied that nanorods were single crystalline and corresponding to interplanar spacing (Cu at. 5, 10, and 15%; 0.56-0.53 nm) can be indexed to the (200) plane of orthorhombic V_2O_5.

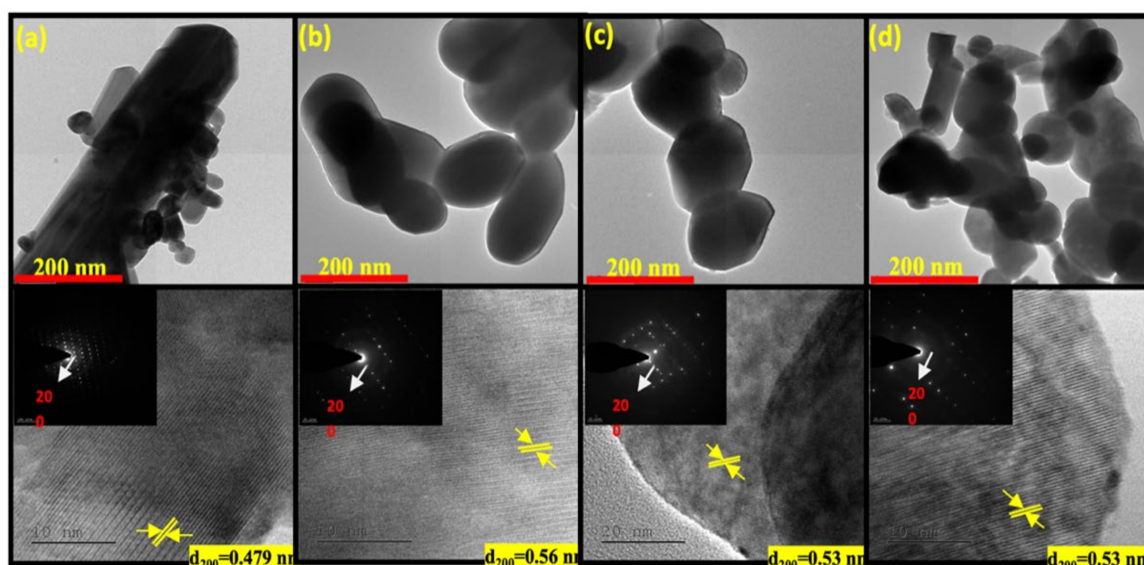

Fig. 3 TEM images of (a) pure and (b-d) $Cu_xV_2O_5$ samples with inset the HRTEM and SAED patterns.

3.4 XPS analysis

Fig. 4(a) depicts the survey spectra of the pure and CVO (Cu at.15%) samples in a wide energy range and the presence of elements V, Cu, O, and C. The narrower scans and peaks-fitted analysis of C1s, $V2p_{1/2}$, $V2p_{3/2}$ and O1s for the V_2O_5 sample are carried out for the respective chemical states and their investigated data are depicted in Fig. 4(b). The two sharp vanadium binding energy peaks of $V2p_{1/2}$ and $V2p_{3/2}$ are centered at 524.47 and 517.04 eV, which are characteristic of V^{5+} oxidation states and demonstrate the production of V_2O_5.

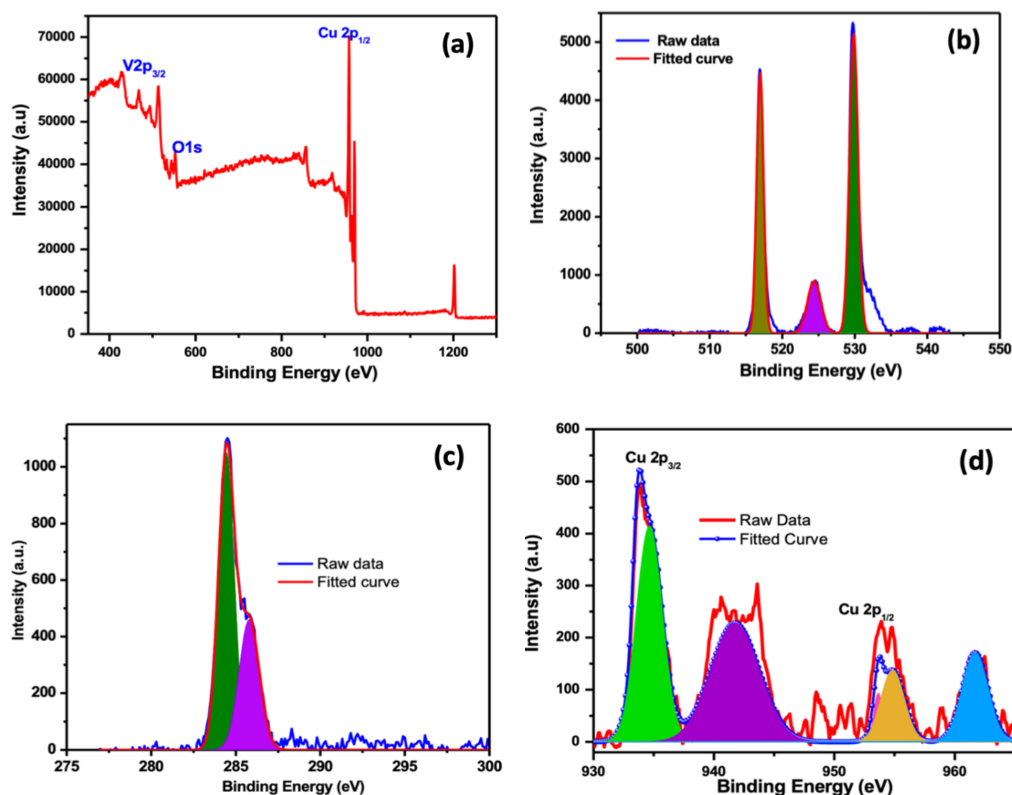

Fig. 4. XPS spectra of (a) survey scan, (b) V2p, O1s, (c) C1s level and (d) Cu2p level.

The O1s peak at 530.94 eV is attributed to the V-O stretch in V_2O_5 in concurrence with the previous detailed literature [33]. Fig 4(c) shows the C1s peak of the XPS data due to carbon contamination, it is frequently used to calibrate peak positions. The sites of the XPS peaks are accurate with the C1s core level at 285 eV as the binding energy (BE) reference. Fig. 4(d) presents the Cu2p core level spectra of the CVO sample, which comprised two peaks of $Cu2p_{3/2}$ and $Cu2p_{1/2}$. Further, the abundance of literature survey reports the BEs of $Cu2p_{3/2}$ in metallic and cationic Cu species have the following ranges: 932.6 eV, 932.5 eV, 933.6 eV for Cu^0, Cu^+, $Cu^{2+,}$ respectively. In general, the elimination of the deterioration that occurs when the copper electronic arrangement is unsaturated d9 (Cu^{2+}), permitting p-d hybridization, results in the appearance of two extra satellite bands in the 941-946 eV and 961-965 eV. Further, Cu^{2+} has a high BE satellite peak involving 940 and 945 eV, which varied from Cu^o and Cu^+ in a sense related to the occurrence of Cu 3d hole states (Cu 3d9), while Cu^0 and Cu^{+1} confirm no similar satellite peak. Cu ions are thereby doped into the V^{5+} sites, despite the fact that the Cu has a mixed state of +1 and +2 valence. Notably, in the case of the Cu concentration at 15%, the peaks are nearly symmetrical at 933.7 and 953.8 eV for BEs of $Cu2p_{3/2}$ and $Cu2p_{1/2}$, indicates that the oxidation state of copper in the sample is 2+ [34].

3.5 Photoluminescence analysis

Figure 5 depicts the photoluminescence spectra of pure and CVO samples recorded from 400 to 700 nm, along with an inset band level diagram. The PL emission spectrum of V_2O_5 shows three major bands associated with a strong blue emission at 418 nm, a blue-green emission at 453 nm, and a broad green emission at 553 nm. The peak at 453 nm is thought to be the result of an electronic transition from the shallow donor level of vanadium interstitials to the valence band, whereas the peak at 418 nm is thought to be the result of an electronic transition from vanadium interstitial to the valence band. Furthermore, the green emission, which is created by point defects, is caused by the radial recombination of a photogenerated hole with an electron from a singly ionized oxygen vacancy. The slight shifting in the band edge peak confirmed the existence of

doping states of V_2O_5. The peaks are in a similar position, but their intensities are significantly different. Under light irradiation, the lower PL intensity may suggest a reduced rate of electron and hole recombination. The photoluminescence of V_2O_5 is well known for being sensitive to the flaws in the studied materials.

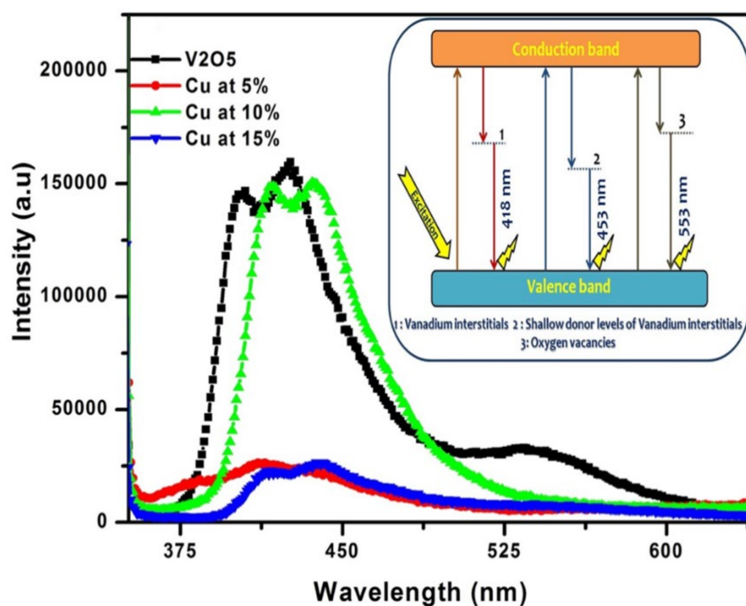

Fig. 5 PL spectra of pure and $Cu_xV_2O_5$ samples.

3.6. Fabrication

The nebulizer spray deposition method has been employed for the growth of CVO thin film on p-Si (100-oriented with a resistivity of 0.8-1.2 Ω cm) substrate. Before the deposition, the Si substrate was cleaned by boiling for 15 minutes and then for another 15 minutes at 50°C. Then, a buffered solution HF: H_2O (1:7) was used to get rid of the natural oxide from the Si substrate. Afterward, the samples were consecutively cleaned for 10 min by boiling acetone, ethanol, and deionized water using ultrasonic vibrations.

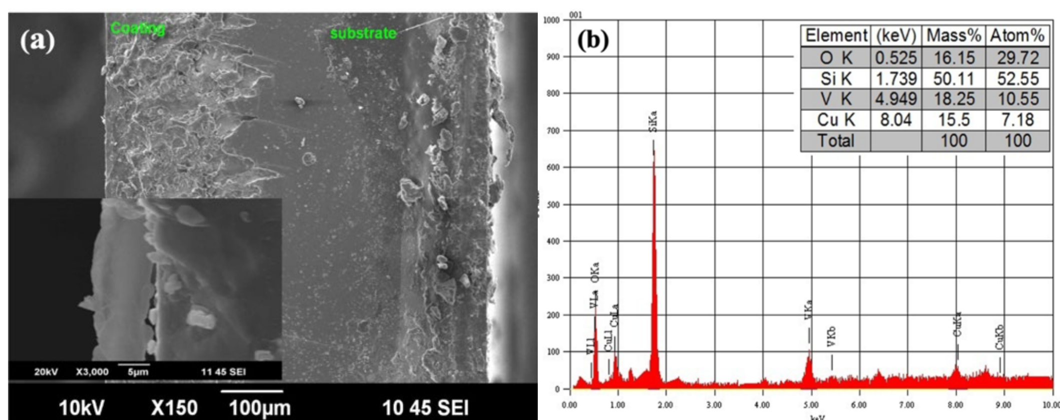

Fig. 6 Shows the SEM cross-sectional image of (a) $Cu_{x=15\%}V_2O_5$/p-Si and (b) EDS spectra.

For fabricating n-V_2O_5/p-Si, the nebulizer spray technique was employed in detail elsewhere [35]. In Fig. 6(a-b) illustrates the cross-sectional image view on SEM and EDS spectra with an inset table for CVO/p-Si (Cu. at. 5%) diode. For V-I measurements, circle-shaped silver contacts were used as electrodes of the studied diodes in front and back surfaces, as shown in inset Fig. 9(a).

3.7. V-I characteristics of CVO/p-Si diodes

Fig. 7 (a-f) shows the forward and reverse biased voltage (V) - current (I) characteristics of the Ag/n-V_2O_5/p-Si/Ag and Ag/CVO/p-Si/Ag junction diodes at room temperature under dark and illumination conditions. The asymmetric and non-ohmic conduct of all V-I characteristics is exposed under dark conditions. In the figure, it can be observed that after illuminating the applied voltage, the forward bias condition does not change significantly. Under light irradiation, the photo-generated holes move to the surface and discharge the negatively charged oxygen ions via surface recombination, leaving electrons with a significant increase in electrical conductivity. When a diode is illuminated, photons with higher photon energies than the band gap of the semiconducting material are absorbed, resulting in the formation of e-h pairs in the depletion region. Such a roll evolution leads to the rise of photocurrent along the reverse bias path. According to these figures, it is seen that the current in the lower voltage region changes exponentially with the applied voltage, according to the linear parts of the forward bias current vs. voltage charts. At higher voltage, the exponential rise begins to deteriorate because of the series resistance effect, which occurs as a result of the depletion layer at the interfaces being minimized. From the I-V characteristics were linear at a more significant bias applied voltage; subsequently, the depletion layer shrinks at the junction interface. In this regard, the examined diodes have a weak voltage dependency for the reverse bias current, while the forward bias current increases exponentially, which is the characteristic property of remedying nature. In the case of the forward bias applying to the Ag/Cu:V_2O_5/p-Si/Ag junction diodes, the exponential rise in current was experiential at low voltage owing to the decrement of the width of the depletion layer at the interface. From the I–V characteristics [36-38], the conventional diode equation (1) can be used to analyze it.

$$I = I_o\left[exp\left(\frac{q\,(V-IR_S)}{nkT}\right)-1\right] \qquad (1)$$

where, V, Rs and n are the applied bias voltage, series resistance and ideality factor while q, k and T are the electronic charges (in C), Boltzmann's constant and absolute temperature in Kelvin, respectively. The examined diodes can be defined using the above Eq. (6), which is an appropriate example for the narratives of Schottky diodes. This consents for a direct assessment of the attained diode parameters. The saturation current (Io) is calculated when V = 0 from the straight-line intercept of ln I, using Eq. (2) given below

$$I = AA^{*}T^{2}exp\left(-\frac{q\,\Phi_B}{kT}\right) \qquad (2)$$

where, A* denotes the effective Richardson constant for p-Si, which is 32 A/cm^2K^2 [39], A is the rectifier contact area and Eq. (2) can be used to determine barrier height (Φ_B). The ideality factor (n) can be determined from the slope's straight-line region in the forward bias ln (I)-V plot and represented as

$$n = {}^{q}/_{kT}\left[{}^{dV}/_{d(InI)}\right] \qquad (3)$$

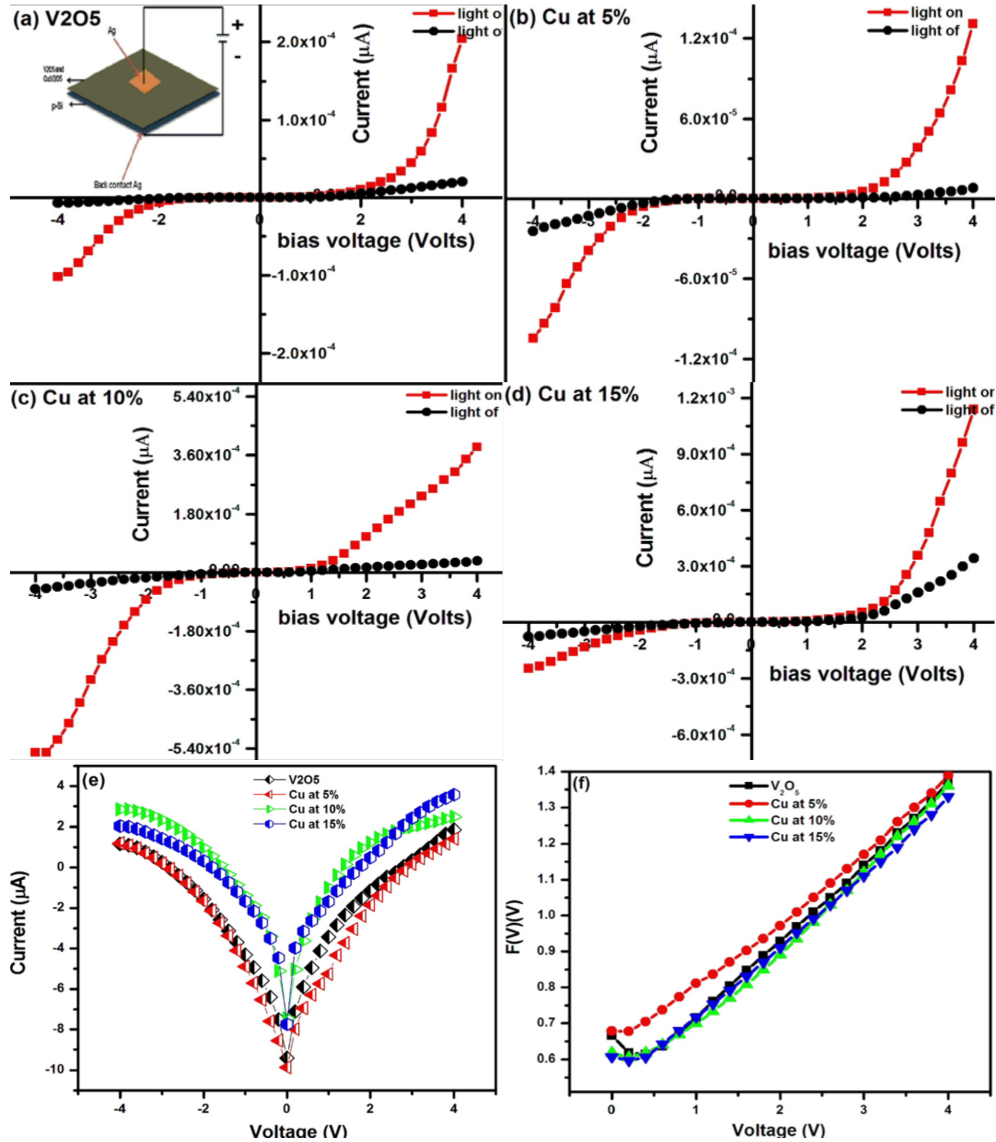

Fig. 7. I-V characteristics of (a) V_2O_5/p-Si with inset of the device structure, (c-d) $Cu_xV_2O_5$/p-Si, (e) current density-voltage plots of $Cu_xV_2O_5$/p-Si and (f) F(V)-V plot $Cu_xV_2O_5$/p-Si.

Table 2 shows the results of estimating the experimental values of barrier height and ideality factor using the current axis intercept and liner region slope of the forward biased semi-log J-V curve. As shown in the table, Cu:V_2O_5/p-Si diodes have a lower ideality factor and a higher barrier height than undoped n-V_2O_5/p-Si diodes. The increase in barrier height could be due to Cu ion insertion in the V_2O_5 lattice, which reduces oxygen vacancies and results in a lower density of free carriers. This raises the barrier height even more at the interface. However, the reduced leakage current in V_2O_5 could be attributed to a decrease in oxygen vacancies. The determined n value attributes the subsequent conditions to the recombination and diffusion processes in these diodes, and the decline in ideality factor can be attributed to the doped diodes with enhanced interface state.

Table 2. Calculated the electrical parameters of pure and $Cu_xV_2O_5$/p-Si diodes.

$Cu_xV_2O_5$ (where x=0, 5, 10 and 15%)	Ideality factor (n)	Barrier height (Φ_B) (eV)	Saturation current (I_s) (A)	Norde function	
				Φ_B (eV)	R_s (kΩ)
00	3.618	0.4123	1.05×10^{-4}	0.423	2.49
05	3.050	0.4262	4.82×10^{-5}	0.471	5.78
10	2.567	0.4345	1.42×10^{-4}	0.461	5.13
15	2.425	0.4027	4.19×10^{-4}	0.433	5.12

In comparison to an ideal one, all of the computed values of 'n' are relatively high. These larger 'n' values could be attributed to recombination in the space-charge region via mid-gap traps. This heterojunction's ideality factor is significantly higher than the unity. The following causes are likely to be responsible for the deviation of the determined 'n' from the ideal one:

I. The nonuniformity of the barrier height

II. Several current routes are available between the interfaces due to the existence of surface states at the junction.

As a result, the current transport mechanism would be successfully regulated. In addition, Norde developed a new characterization approach to determine the barrier height (Φ_B) and series resistance (Rs) of the device [35]. F(V) vs. V graphs of undoped and Cu-doped V_2O_5/p-Si diodes are shown in Fig. 7(f) and their projected values are reported in Table 2. The discrepancy between Φ_B values derived using Norde and I-V methods can be seen in this regard. This is because high series resistance can avoid an accurate barrier height evolution from typical V-I plots. It is clear that the studied diodes demonstrated well-rectifying behaviour, which is primarily due to the generated e-h pairs, and these charges contribute to the photocurrent as a result of light absorption. It means that the rectification effect has been reduced, and the diodes exhibit extra-perfect behaviour when exposed to light. Furthermore, A widely used tool for analyzing the transport mechanism is the ratios of photocurrent to dark current with time-dependent data. The studied device was maintained in the dark for 15 minutes before the experiment to stabilize the current at a consistently applied potential. The transient photocurrent varied with the intensity of light, as seen in Fig. 7(a-d). When the light was turned on, the current increased to a specific value and then decreased to its initial value when the light was turned off. The rise in photocurrent confirmed that more free charge carriers were created depending on light intensity. On the other hand, the decrease in photocurrent established that the free charge carriers are reduced more depending on trap levels. Furthermore, due to charge carrier entrapment in the deep layers of dark environments, the current returns to its initial state. When compared to the undoped n-V_2O_5/p-Si diode, the amount of photocurrent increases as Cu^{2+} content increases. As a result, photodiodes with varied Cu^{2+} concentrations are observed to exhibit photoconduction behavior.

4. Conclusions

A systematic study was conducted on CVO nanorods produced using the wet chemical method with various dopant concentrations. Observations revealed that annealing pure and doped samples at 600°C changed the corresponding phase to orthorhombic. The crystalline sizes are reduced relatively with increasing the Cu^{2+} doping levels. SEM analysis revealed that increasing Cu^{2+} contents caused a change from nanorods to disk shape morphology of V_2O_5. PL results represent that as the Cu content in Cu:V_2O_5 samples increases, the UV emission peak shifts to a longer wavelength. The electrical properties of the Cu:V_2O_5/p-Si diode improved with increasing copper concentration due to increased charge carrier concentration and decreased defect states in V_2O_5 nanorods, as demonstrated by I-V features and diode performance evaluation. This study provides a promising avenue for the fabrication of Cu:V_2O_5/p-Si heterojunction structures, which are thought to be viable candidates for photoresponse activities

References

[1] Top Khac Lea, Manil Kang, Sok Won Kim, Ceramics International, 45, 15781–15798, (2019); https://doi.org/10.1016/j.ceramint.2019.05.339
[2] T. Zhai, H. Liu, H. Li, X. Fang, M. Liao, L. Li, H. Zhou, Y. Koide, Y. Bando, D. Golberg, Adv. Mater, 22, 2547–2552, (2010); https://doi.org/10.1002/adma.200903586
[3] V. Balasubramani, J. Chandrasekaran, R. Marnadu, P. Vivek, S. Maruthamuthu, S. Rajesh,I J. Inorg. Organomet. Polym. Mater, 29, 1533, (2019); https://doi.org/10.1007/s10904-019-01117-z
[4] R. Marnadu, J. Chandrasekaran, M. Raja, M. Balaji, S. Maruthamuthu, P. Balraju, Superlattices Microstruct, 119, 134, (2018); https://doi.org/10.1016/j.spmi.2018.04.049
[5] R. Marnadu, J. Chandrasekaran, S. Maruthamuthu, V. Balasubramani, P. Vivek, R. Suresh, Appl. Surf. Sci., 480, 308, (2019); https://doi.org/10.1016/j.apsusc.2019.02.214
[6] M. Chiranjeevi, Guruviah Velmathi.. International Journal of Applied Science and Engineering, 19, 2021220 (2022); https://doi.org/10.6703/IJASE.202203_19(1).005
[7] S. Kamila, V. R. Venugopal, International Journal of Applied Science and Engineering, 14, 133–146 (2017); https://doi.org/10.6703/IJASE.2017.14(3).133
[8] R. Stanley, A. S.Nesaraj, International Journal of Applied Science and Engineering, 12, 9–21 (2014); https://doi.org/10.6703/IJASE.2014.12(1).9
[9] R. Suresh, S. Subash, K. Thirumal Valavan, M. Justin Paul, T. Indira Priyadharshini, NanoNEXT, 1, 24-29 (2020); https://doi.org/10.34256/nnxt2014
[10] S Yadav, N Ran and K Saini, IOP Conf. Ser.: Mater. Sci. Eng. **1225** 012004 (2022); https://doi.org/10.1088/1757-899X/1225/1/012004
[11] M. Gowtham, N. Senthil Kumar, Chandrasekar Sivakumar, K. Mohanraj, NanoNEXT, 3, 1-7 (2022);. https://doi.org/10.54392/nnxt2221
[12] Xi Zhu, J. Energy Storage, 49, 104148 (2022); https://doi.org/10.1016/j.est.2022.104148
[13] R. Suresh, K. Thirumal Valavan, M. Justin Paul, T. Indira Priyadharshini, NanoNEXT, 1, 1-9 (2020); https://doi.org/10.34256/nnxt2011
[14] V. Modafferi, S. Trocino, A. Donato, G. Panzera, G. Neri, Thin Solid Films, 548, 689–694, (2013); https://doi.org/10.1016/j.tsf.2013.03.137
[15] V. Parvulescu, S. Boghosian, V. Parvulescu, S. Jung, P. Grange, J. Catal, 217, 172–185, (2003); https://doi.org/10.1016/S0021-9517(03)00028-9
[16] G. Rizzo, A. Arena, A. Bonavita, N. Donato, G. Neri, G. Saitta, Thin Solid Films, 518, 7124–7127, (2010); https://doi.org/10.1016/j.tsf.2010.07.010
[17] G.D.J. Smit, S. Rogge, T.M. Klapwijk, arXiv preprint cond-mat, 110256, (2011); https://doi.org/10.1016/j.sna.2016.09.001
[18] L. Vikas, K. Vanaja, P. Subha, M. Jayaraj, Sens. Actuators A: Phys, 242, 116–122, (2016); https://doi.org/10.1016/j.sna.2016.02.038
[19] M. Rajabi, R. Dariani, A.I. Zad, Sens. Actuators A: Phys., 180, 11–14, (2012); https://doi.org/10.1016/j.sna.2012.04.003
[20] G.M. Ali, J.C. Moore, A.K. Kadhim, C. Thompson, Sens. Actuators A: Phys, 209, 16–23, (2014); https://doi.org/10.1016/j.sna.2014.01.010
[21] R. Suresh, K. Giribabu, R. Manigandan, S. Munusamy, S. Praveen Kumar, S. Muthamizh, A. Stephen, V. Narayanan, J. Alloy. Compound, 598, 151, (2014); https://doi.org/10.1016/j.jallcom.2014.02.041
[22] S.W. Liu, W. Wang, L. Zhou, L.S. Zhang, J. Cryst. Growth, 293, 404, (2006); https://doi.org/10.1016/j.jcrysgro.2006.05.045
[23] R. Suresh K. Giribabu R. Manigandan S. Praveen Kumar S. Munusamy S. Muthamizh A. Stephen V. Narayanan, Sensor. Actuat. B: Chemical, 202, 440, (2014); https://doi.org/10.1016/j.snb.2014.05.095
[24] S. Zhan, Y. Wei, X. Bie, C. Wang, F. Du, G. Chen and F. Hu, J. Alloy. Comp, 502, 92, (2010); https://doi.org/10.1016/j.jallcom.2010.03.133
[25] R. Abaira, T. Dammak, A. Matoussi and A. Younes, Superlattice. Microst, 91, 365, (2016); https://doi.org/10.1016/j.spmi.2016.01.008
[26] D. Zhu, H. Liu, L. Lv, Y. D. Yao and W. Z. Yang, Scripta Mater, 59, 642, (2008); https://doi.org/10.1016/j.cep.2017.07.019

[27] Q. Song, H. Pang, W. Gong, G. Ning, Y. Zhang, X. Cheng and L. Yuan, Mater. Lett, 161, 244, (2015); https://doi.org/10.1016/j.matlet.2015.08.070
[28] R. Suresh, K. Giribabu, R. Manigandan, S. Munusamy, S. Praveen Kumar, S. Muthamizh, J. Alloy. Comp., 598, 151, (2014); https://doi.org/10.1016/j.jallcom.2014.02.041
[29] Yadav, D, Varshney, J. Supercond. Nov. Magn, 30, 1297, (2017); https://doi.org/10.1007/s10948-016-3931-2
[30] D. Sundeep, T.V. Kumar, A.G. Krishna, R.V.S. S. N. Ravi Kumar, Silicon Publishers, 11, 1517–1524, (2019); https://doi.org/10.1007/s12633-018-9972-3
[31] Y.U. Hua, C. Wen, D. Ying, M. Liqiang, Q. Yanyuan, P. Junfeng, Mater. Sci. Ed, 21, 38, (2006); https://doi.org/10.1007/BF02861466
[32] G. Silversmit, D. Depla, H. Poelman, G.B. Marin, R.D. Gryse, J. Electron. Spectrosc, 135, 167, (2004); https://doi.org/10.1016/j.elspec.2004.03.004
[33] M.C. Biesinger, Surf. Interface. Anal, 49, 1325, (2017); https://doi.org/10.1002/sia.6239
[34] N. Senthil Kumar, M. Sethu Raman, J. Chandrasekaran, R. Priya, Murthy Chavali, R. Suresh, Mater. Sci. Semicond. Proc, 41, 497, (2016); https://doi.org/10.1016/j.mssp.2015.08.020
[35] J. Osvald, E. Dobrocka, Semicond. Sci. Technol., 11, 1198, (1996); https://doi.org/10.1088/0268-1242/11/8/014
[36] K. Mohanraj, D. Balasubramanian, J. Chandrasekaran, A. Chandra Bose, Materials Science in Semiconductor Processing, 79, 74-91, (2018); https://doi.org/10.1016/j.mssp.2018.02.006
[37] N. Senthil Kumar, J.H. Chang, Mon-Shu Ho, Babu Balraj, S. Chandrasekar, B. Mohanbabu, M. Gowtham, Donghui Guo, K. Mohanraj, Journal of Inorganic and Organometallic Polymers and Materials, 31, 1066-1078, (2021); https://doi.org/10.1007/s10904-020-01751-y
[38] Sze SM, Ng KK. Physics of Semiconductor Devices. Hoboken, NJ, USA: John 23 Wiley & Sons, Inc; (2006); https://doi.org/10.1002/0470068329
[39] H. Norde, J. Appl. Phys, 50, 5052, (2008); https://doi.org/10.1063/1.325607